Active tuning of near-infrared interaction of single-walled carbon nanotubes with quasibound states in the continuum in all-dielectric metasurfaces

Peng Xie,[1] Wei Wang,[1] and Yihan Cheng[2,*]
[1]*College of Physics, Sichuan University, Chengdu 610064, China*
[2]*International Center for Quantum Materials, School of Physics, Peking University, Beijing 100871, China*

(Received 10 April 2024; revised 27 June 2024; accepted 24 July 2024; published 6 August 2024)

Single-walled carbon nanotubes (SWCNTs), with their high oscillator strength and large exciton binding energies, are becoming highly promising materials for the study of exciton-polaritons in the near infrared (NIR) at room temperature. However, current SWCNT-based strong coupling systems generally involve either lossy plasmonic nanostructures or bulk cavity-type resonators with poor compactability and tunability. Here, an ultracompact and low-loss all-dielectric metasurface combined with a phase change material (PCM) is proposed to enable active tuning of SWCNT-based exciton-polaritons in the NIR region. We demonstrate control of exciting quasibound states in the continuum (QBICs) by changing temperatures in the metasurface, which enables an active and flexible tuning exciton-QBIC interactions. We reveal that the dominant excitations of the magnetic dipole and high-order electric quadrupole at QBIC resonance play an important role in field enhancement, thus greatly facilitating the exciton-QBIC interaction. A quantum model fully describes the microscopic coupling dynamics, demonstrating a temperature-dependent sub- and superradiance of the polariton states. We also demonstrate a linear dependence of exciton-QBIC coupling strength on the SWCNT concentrations, which may provide an efficient approach for observing ultrastrong coupling phenomena. The PCM-assisted active tuning of exciton polaritons is expected to enable ultrafast and highly compact polariton devices at telecommunication wavelengths.

DOI: 10.1103/PhysRevB.110.075406

I. INTRODUCTION

When confined light interacts strongly with an excitonic resonance, new light-matter quasiparticles called exciton-polaritons can form [1,2]. In this strong coupling regime, the coupling between the excitonic state and the optical excitation exceeds their individual damping rates, and mixed exciton-photon eigenstates arise with the formation of the so-called lower polariton (LP) and upper polariton (UP) [3,4]. Exciton-polaritons possess a mixture of excitonic and photonic properties, allowing for the realization of various phenomena such as Bose-Einstein condensation [5], ultralow threshold lasing [6], the generation of quantum light, quantum simulation [7], and superfluidity [6,8–11].

Typical platforms for launching exciton-polaritons generally involve excitonic emitters with high oscillator strength such as organic semiconductors and two-dimensional transition-metal dichalcogenides. When integrated with various optical nanoresonators such as plasmonic/dielectric nanostructures, Fabry-Pérot cavities, and photonic crystals, the high oscillator strength of excitonic transitions in these materials and the enhanced electric field properties of the optical modes can facilitate a significant boost in strong light-matter coupling with large Rabi splittings [12–17]. Due to the intrinsic responsive wavelength range of the excitonic resonances, strong coupling phenomena in those materials occur only in the visible region, which hinders their potential applications in the near-infrared (NIR) range, where telecommunication and integration with silicon photonics are highly desirable.

In the NIR region, semiconducting single-walled carbon nanotubes (SWCNTs) are becoming promising candidates for the study of strong light-matter interactions due to their unique optoelectronic properties: (1) SWCNTs possess both large exciton oscillator strengths and small Stokes shifts [18,19], (2) SWCNTs exhibiting high exciton binding energies (300 meV) and chiral correlated exciton transition energies crossing the entire near-infrared spectrum provide a platform for tailoring coupling systems with excellent performance [20–22], and (3) SWCNTs show strong high exciton mobility and exciton-phonon coupling, both of which may contribute to the realization of exciton-polaritons [23,24]. Benefiting from these properties of SWCNTs, exciton-polaritons have been demonstrated in a variety of nanoscale devices, such as photonic waveguides, Fabry-Pérot cavities, photonic crystals, and plasmonic crystals [25–31]. These optical resonators, however, typically suffer from weak compactness, poor integration, and high Ohmic losses in plasmonic resonators. More importantly, it is extremely challenging for these nanostructures to achieve active tuning of exciton polaritons, although passive tuning from weak to strong or even ultrastrong coupling by increasing the concentration of SWCNTs has been reported.

In this paper, we propose an ultracompact and low-loss all-dielectric metasurface combined with a phase change

*Contact author: yhcheng@pku.edu.cn

material (PCM) to enable active tuning of SWCNT-based exciton-polaritons in the NIR region, which, to the best of our knowledge, has not been reported so far. Compared to their lossy plasmonic and bulky microcavity counterparts, all-dielectric metasurfaces made by high-refractive-index dielectrics (such as Si, Ge, and TMDC materials) exhibit extremely low loss and low-dimensional geometries, which are greatly favorable for the design of compact polaritonic devices [32–37]. We designed a metasurface supporting bound states in the continuum (BICs). It is a unique optical excitation with an infinite quality Q factor, which can be transformed into quasi-BICs (QBICs) with a finite Q factor to utilize its rich physical properties in practical applications. Such QBIC resonances not only feature extremely low radiative damping rates and large electric field enhancements but also enable simultaneous excitations of different optical modes, such as electric, magnetic, and higher-order electric quadrupoles, compared to other optical resonators described earlier [11,38,39]. With the help of these distinct properties, the QBIC has been exploited extensively for enhancing light-matter interactions and tailoring the properties of matter, such as fluorescence enhancement [40], polaritons lasers [41], enhanced nonlinear harmonic generation [34], and strong coupling phenomena [42–45].

With the help of VO_2, a widely used PCM offering significant temperature-dependent refractive index differences, we demonstrate control of QBIC excitation by changing the temperature, which enables an active and flexible tuning of exciton-QBIC interactions. We employ a multipole expansion approach combined with near-field analysis, revealing that the dominant excitations of the magnetic dipole and high-order electric quadrupole at QBIC resonance play an important role in field enhancement, thus greatly facilitating the exciton-QBIC interaction. We also utilize a quantum model to fully describe the microscopic coupling dynamics, demonstrating temperature-dependent sub- and superradiance of the polariton states. We also demonstrate a linear dependence of the exciton-QBIC coupling strength on the SWCNT concentrations, which may provide an efficient approach for observing ultrastrong coupling phenomena.

II. RESULTS AND DISCUSSION

A. The strong coupling system

The proposed metasurface, shown in Fig. 1(a), consists of a 10-nm-thick VO_2 film embedded in the middle of silicon nanorods. The metasurface is then covered by a thin SWCNT film. The unit cell of the Si-VO_2 metasurface (top view) is given in Fig. 1(b) with detailed geometrical parameters. Here, an asymmetry parameter θ is defined as the rotation angle of the neighboring nanorod with respect to the y axis. Such all-dielectric metasurfaces with rich optical properties can be fabricated by high-precision parameter-controlled electron beam lithography or reactive ion beam etching techniques.

To study the QBIC-exciton interactions, we first simulate the static spectral response of the hybrid system by using the finite-difference time-domain method. In our simulations, the periodic boundary conditions are applied in the x and y directions, while the z direction is set as perfectly matched layer conditions to prevent unphysical reflections. We mesh

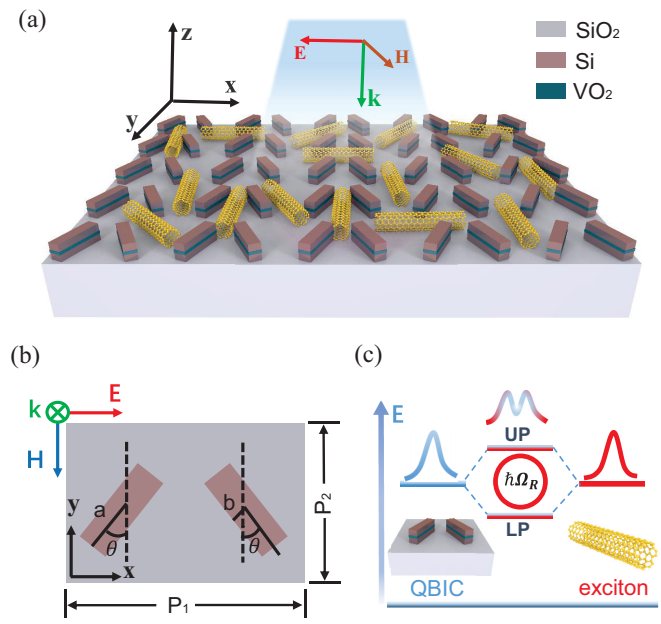

FIG. 1. (a) Three-dimensional schematic of the coupling system: Si-VO_2 metasurface overlaid by a layer of random (6,5) SWCNTs. The thickness of the VO_2 film is 10 nm. (b) Parametric layout of the $x-y$ plane of the Si-VO_2 metasurface. The semimajor axis a and semiminor axis b are 250 and 90 nm, respectively. Period P_1 (x direction) and period P_2 (y direction) are 535 and 400 nm, respectively. The thickness of Si is 150 nm, and the center spacing in elliptical Si is 267.5 nm. (c) Schematic diagram of the created polaritons (UP and LP) via the interaction of excitons with QBICs modes.

the entire simulation area in $1 \times 1 \times 1$ nm^3 to obtain an accurate spectral response of the coupled system. We employ a plane wave polarized along the x axis to illuminate the hybrid system at normal incidence, as shown in Fig. 1(a). The refractive indices of Si and SiO_2 are $n_{Si} = 3.5$ and $n_{SiO_2} = 1.46$, respectively. The real and imaginary parts of the refractive indices of VO_2 at 30 °C and 80 °C were obtained from Ref. [46]. The dielectric function of high-purity SWCNTs with a concentration of 0.46 wt % encapsulated by the poly[(9,9-dioctylfluorenyl-2,7-diyl)-alt-co-(6,6′-(2,2′-bipyridine))] (PFO-BPy) is expressed by the classical Lorentz oscillator as [27]

$$\epsilon(E) = \epsilon_B + \frac{f\omega_X^2}{\omega_X^2 - \omega^2 - i\omega\Gamma_X}. \quad (1)$$

Here, $\epsilon_B = 2.78$ represents the background permittivity, and $\hbar\omega_X = 1.246$ eV is the transition energy. $f = 0.003$ and $\hbar\Gamma_X = 20$ meV are the oscillator strength and full linewidth of the exciton resonance in SWCNTs. All the parameters of the SWCNT are obtained using Eq. (1) in the next section unless otherwise stated.

Figure 1(c) shows a schematic of the interaction between QBIC modes and excitons. It can be clearly seen that the UP and LP with both QBIC mode properties and exciton properties are formed when the exciton is coupled to the QBIC mode. For the present coupling system, we obtain the spectral properties of the hybrid system with the anticrossing phenomenon by varying the asymmetric parameter θ, which is characterized by the Rabi splitting $\hbar\Omega_R$.

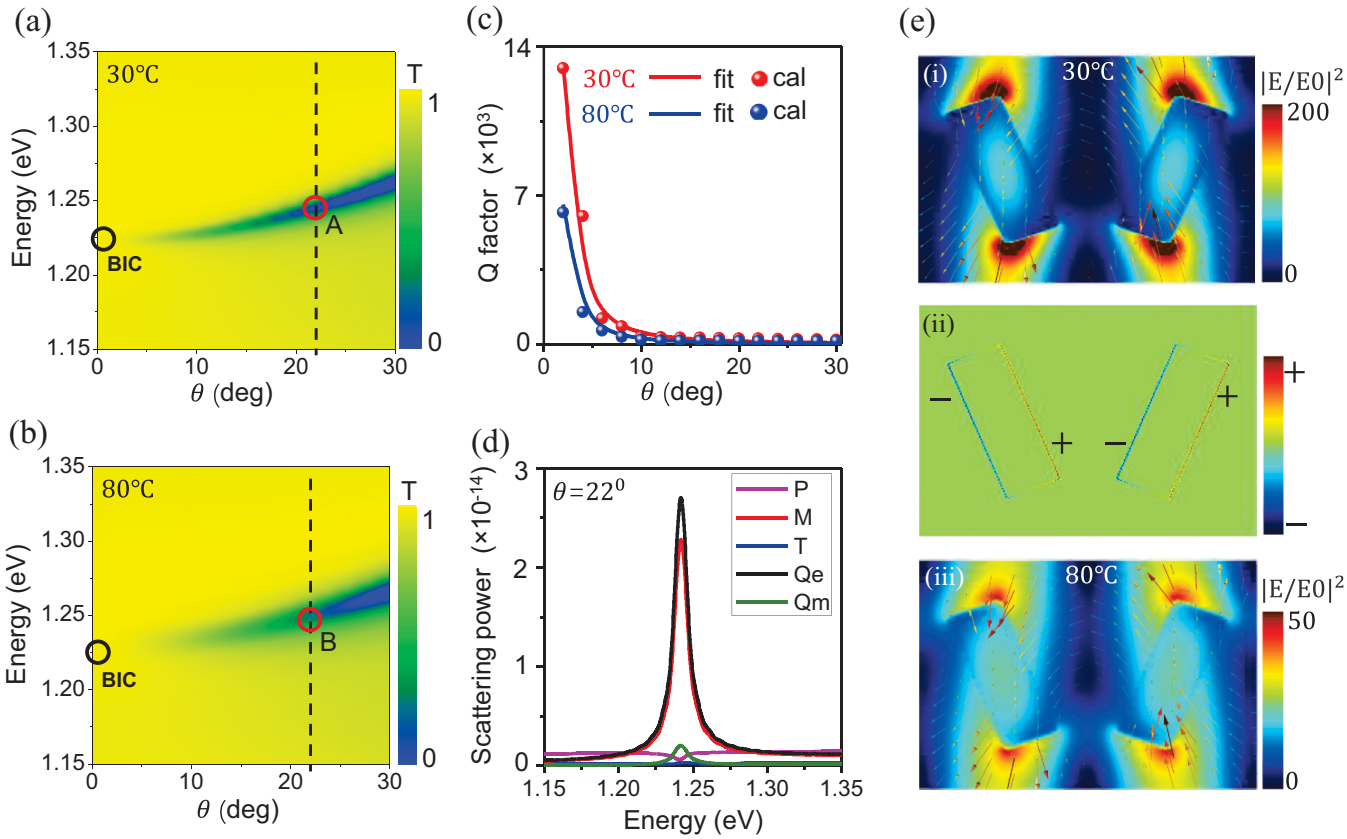

FIG. 2. Transmission spectrum of the metasurface at (a) 30 °C and (b) 80 °C. (c) Calculated and fitted Q factors of the metasurface as a function of the angle at 30 °C (red) and 80 °C (blue). (d) Scattering contributions of different multipoles from the unit cell of the metasurface at an angle of $\theta = 22°$. P, M, T, Qe, and Qm represent the electric dipole, magnetic dipole, toroidal dipole, electric quadrupole, and magnetic quadrupole responses, respectively. (e) Electric field distribution and charge distribution in the $x-y$ plane for a unit cell on a metasurface.

B. Optical properties of metasurfaces at different temperatures

We first explore the optical properties of the Si-VO_2 metasurfaces at different temperatures in the absence of SWCNTs. Figures 2(a) and 2(b) give the simulated transmission spectrum of the 2D metasurface while varying the asymmetric parameter θ from 0° to 30° at 30 °C and 80 °C, respectively. Transitions from the symmetry-protected BIC (black circle) to the QBIC mode can clearly be seen as a direct consequence of the symmetry breaking in the $x-y$ plane. In addition, the damping rate of the QBIC mode at 80 °C (peak B) is faster than that at 30 °C (peak A), which arises from the temperature-dependent changes in the real and imaginary parts of VO_2, which are as high as $\Delta_n \approx 1.2$ and $\Delta_k \approx 1.1$ for 30 °C and 80 °C, respectively. This feature can be demonstrated by the Q factor as a function of the asymmetric parameter α, as shown in Fig. 2(c). We calculate here the Q factor (defined as ω/γm where ω is the resonant frequency and γ is the damping rate) of the metasurface only for larger θ. Since the amplitude of the QBIC mode is very small when θ is small, it is difficult to obtain an accurate Q factor. Two aspects can be seen: (1) the dependence of the Q factor on the asymmetry parameter follows $Q \propto 1/\alpha^2$ ($\alpha = \sin\theta$) [47], which is in accordance with the typical quadratic inverse law for all symmetry-breaking meta-atomic designs, and (2) importantly, the Q factors at 30 °C are higher than those at 80 °C, particularly for small values of the asymmetric parameter α.

To get deep insight into the optical properties of the Si-VO_2 metasurfaces, we evaluate the contributions of different multipole components in the QBIC mode using a multipole expansion method in the Cartesian coordinate system. The details of the multipole expansion approach can be found in Ref. [48]. Taking the optical response at 80 °C as an example, we demonstrate the scattering power for each multipole component corresponding to peak B with $\theta = 22°$, as shown in Fig. 2(d). Obviously, the magnetic dipole (M) and the electric quadrupole (Qe) are dominate in the present QBIC mode. The contributions of scattering power from the electric dipole (P), toroidal dipole (T), and magnetic quadrupole (Qm) are very weak.

Near-field analysis further confirms the domination of M and Qe. As shown in Fig. 2(e), plots (i) and (iii), the counterclockwise distribution of the displacement currents creates a clear magnetic dipole along the z direction at peak A for both 30 °C and 80 °C. The charge distribution [Fig. 2(e), plot (ii)] at peak B for 80 °C exhibits the typical feature of the electric quadrupole dipole [33]. More importantly, the maximum enhancement of the electric field at peak A for 30 °C [Fig. 2(e), plot (i)] is about 4 times stronger than that at peak B for 80 °C [Fig. 2(e), plot (iii)]. This aspect is critical for the

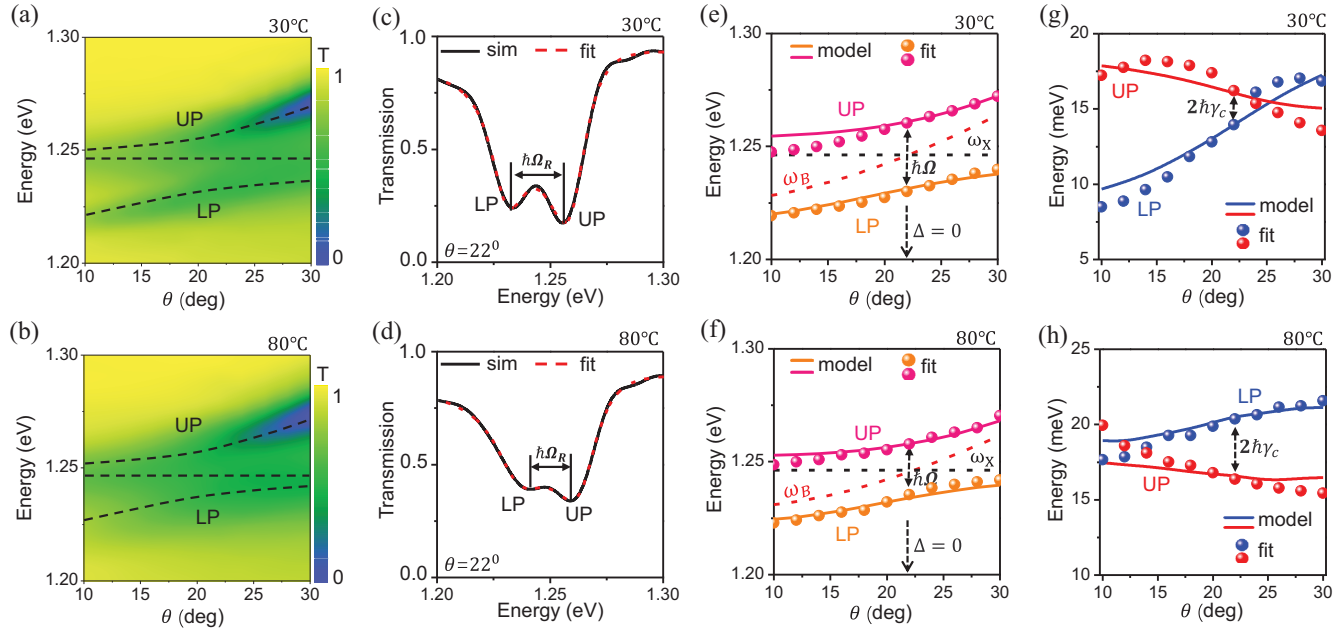

FIG. 3. Transmission spectrum of the coupling system as a function of the asymmetric parameter θ (in color scale) at (a) 30 °C and (b) 80 °C. Simulated (black solid line) and fitted (red dotted line) transmission spectrum at (c) 30 °C and (d) 80 °C for the coupled system at zero detuning ($\theta = 22°$). Dispersion curves of the coupled system at (e) 30 °C and (f) 80 °C obtained with the model (solid lines) and fitting spectra (spheres). The red and black dashed lines represent the dispersion of the QBIC mode and exciton resonance, respectively. Spectral full widths at half maximum (FWHM) at (g) 30 °C and (h) 80 °C for the coupled system obtained with fitting (spheres) and the model (solid lines).

dynamic tuning of the coupling strength, which will be discussed later.

C. Temperature-dependent coherent and incoherent interactions between QBICs and excitons

We now start to investigate the QBIC-exciton interaction process by depositing the SWCNT film on top of the metasurface. Figures 3(a) and 3(b) give the simulated transmission spectra (in color scale) as a function of the asymmetric parameter β for 30 °C and 80 °C, respectively. Anticrossing phenomena can be seen in the spectra, as marked by the black dashed lines, indicating the occurrence of QBIC-exciton interactions.

To quantitatively describe the optical response of the coupled system, we extract the dispersion and spectral features of the emerging polariton modes with high accuracy by fitting the simulated transmission spectrum to a Fano-shaped line shape. The asymmetric Fano-shaped transmission spectrum $T(\omega) = |t(\omega)|^2$ at different temperatures can be described as [4]

$$t(\omega) = a_b + \sum_{j=\mathrm{UP,LP}} \frac{b_j \gamma_j e^{i\phi_j}}{\omega - \omega_j + i\gamma_j}, \tag{2}$$

where a_b and b_j represent the background amplitude and the amplitude of the transmission spectrum of the hybrid states. ϕ_j is the spectral phase. The resonance energy and full width at half maximum (FWHM) of the polariton states are ω_j and $2\gamma_j$. Figures 3(c) and 3(d) plot the simulated (black solid line) and fitted (red dashed line) transmission spectra of the coupled system for 30 °C and 80 °C at zero detuning ($\theta = 22°$), respectively. The fitting results match well with the calculated transmission spectra of the polariton states. The Rabi splitting $\hbar\Omega_R$, defined as the peak-to-peak distance between the UP and LP resonant frequencies, is roughly estimated to be $\hbar\Omega_R = 28$ meV (30 °C) and $\hbar\Omega_R = 21$ meV (80 °C). There are two reasons for the difference in Rabi splittings for different temperatures: (1) the electric field strength of the metasurface for 30 °C is greatly enhanced compared to that for 80 °C, as demonstrated in the previous section, and (2) importantly, the FWHM of the metasurface and the damping rate of the exciton are less different for 30 °C than for 80 °C.

We further extract the fitted dispersion relation of the UP and LP as a function of the asymmetric parameter θ for different temperatures in Figs. 3(e) and 3(f) and the FWHM in Figs. 3(g) and 3(h). The fitted dispersion lines show significant anticrossing behavior, where the Rabi splittings of the coupled system for different temperatures can be evaluated at zero detuning (black dashed arrows). Surprisingly, the FWHMs of the UP and LP exhibit significant differences at zero detuning for both 30 °C and 80 °C, which indicates that coherent interactions cause incoherent coupling processes and thus ultimately contribute to the formation of sub- and superradiative polariton states. We notice, however, that the incoherent coupling strength $\hbar\gamma_c$ of the coupled system for 30 °C is much smaller than that for 80 °C, which will be explained in the following discussion.

To quantitatively describe the present coherent and incoherent coupling properties of the coupling system at different temperatures, we employ the widely used coupled oscillator

model with a non-Hermitian Hamiltonian containing both coherent and incoherent coupling terms, which can be expressed as [4]

$$\hbar\left(\begin{bmatrix}\widetilde{\omega}_Q & g\\ g^* & \widetilde{\omega}_X\end{bmatrix}-i\begin{bmatrix}0 & \gamma_c\\ \gamma_c & 0\end{bmatrix}\right)\begin{pmatrix}\alpha\\ \beta\end{pmatrix}=E\begin{pmatrix}\alpha\\ \beta\end{pmatrix}, \quad (3)$$

where $\widetilde{\omega}_{\mathrm{Q}}=\omega_{\mathrm{Q}}-i\gamma_{\mathrm{Q}}$ and $\widetilde{\omega}_{\mathrm{X}}=\omega_{\mathrm{X}}-i\gamma_{\mathrm{X}}$ are the complex resonance frequencies of the QBIC and the exciton resonance, respectively. α and β represent the Hopfield coefficients of the subsystem, which satisfy $|\alpha|^2+|\beta|^2=1$. The dispersion and damping rate of the polarization modes can be given by the real and imaginary parts of the complex eigenvalues:

$$E_{\pm}=\hbar\widetilde{\omega}_{\pm}=\hbar\left(\frac{\widetilde{\omega}_{\mathrm{Q}}+\widetilde{\omega}_{\mathrm{X}}}{2}\right)\pm\hbar\sqrt{\left(\frac{\widetilde{\omega}_{\mathrm{Q}}+\widetilde{\omega}_{\mathrm{X}}}{2}\right)^2+\left(|g|^2-{\gamma_c}^2\right)-2i\gamma_c\mathrm{Re}(g)}. \quad (4)$$

The calculated dispersion relation [solid lines in Fig. 3(e)] and FWHM [solid lines in Fig. 3(g)] of the UP and LP branches for 30 °C are perfectly reproduced by diagonalizing Eq. (3) with optimal coherent coupling strength $\hbar g=$ 14 meV and the cross-damping term $\hbar\gamma_{\mathrm{c}}=0.4$ meV, as well as $\hbar g=10.5$ meV and $\hbar\gamma_{\mathrm{c}}=1.2$ meV for 80 °C [solid lines in Figs. 3(f) and 3(h)]. It is obvious that the coupling strength of the coupled system increases as the temperature decreases. In addition to the enhanced coherent coupling strength for 30 °C compared to that for 80 °C, we also note that the cross-damping term $\hbar\gamma_{\mathrm{c}}$ decreases rapidly from 1.2 down to 0.4 meV. This incoherent coupling pathway is microscopically formed by the spontaneous emission of photons from one subsystem into a vacuum continuous medium reservoir that are subsequently reabsorbed by the other subsystem without preserving any phase relationship. Such incoherent coupling pathways induced by coupling ultimately result in the formation of sub- and superradiative hybrid modes, which are capable of modulating the radiative damping rate. It is associated with the radiative damping rate of the subsystem ($\gamma_{\mathrm{Q,rad}}$, $\gamma_{\mathrm{X,rad}}$) and the inner product of the unit vector of the dipole moment ($\hat{\boldsymbol{\mu}}_{\mathrm{Q}}$, $\hat{\boldsymbol{\mu}}_{\mathrm{X}}$) of the subsystem, i.e., $\gamma_c\leqslant\sqrt{\gamma_{\mathrm{Q,rad}}\gamma_{\mathrm{X,rad}}}(\hat{\boldsymbol{\mu}}_{\mathrm{Q}}\cdot\hat{\boldsymbol{\mu}}_{\mathrm{X}})$. For the present coupling system, it is reasonable to assume that the dipole moments of the subsystems are stable. We therefore deduce that the decrease in the incoherent coupling strength stems from the fastening of the radiative damping rate of the QBIC mode for 80 °C compared to that for 30 °C. Such active modulation of coherent and incoherent coupling processes between subsystems by phase change materials provides us with excellent convenience in designing ultrasensitive, tunable polaritonic devices.

D. Coupling dynamics: Heisenberg-Langevin formalism

In order to deeply investigate the microscopic coupling process of the QBIC-exciton interaction, we utilize a full quantum model to quantitatively describe the spectral response and coupling dynamics of the hybrid system. In the present case, the QBIC and exciton are considered to be a bosonic system and a Fermi system, respectively. Their interaction processes are modeled in the framework of the Heisenberg-Langevin form as [49]

$$\dot{\hat{a}}=-(i\Delta_Q+\gamma_Q)\hat{a}-(ig+\gamma)\sigma_-+\sqrt{\Gamma_Q}A_Q+\hat{F}_Q,$$
$$\dot{\sigma}_-=-(i\Delta_X+\gamma_X)\sigma_--(ig^*+\gamma)\hat{a}-A_X\sigma_z+\hat{F}_X. \quad (5)$$

Here, $\dot{\hat{a}}$ and $\dot{\sigma}_-$ represent the complex modal coefficients of the QBIC and exciton, respectively. A_Q and A_X are coupling efficiencies originating from the interaction between the driving field and the subsystems. g and γ represent the coherent coupling strength and incoherent damping rate of the QBIC and exciton interaction, which are due to the direct coupling between subsystems and the interaction between subsystems and the continuum reservoir. It is interesting to note that the coherent coupling strength g is typically a complex quantity, i.e., $g=ge^{i\phi}$, with ϕ representing the Rabi phase, which describes the initial spatial distance between two subsystems and the resulting relative phase difference. It is a critical factor in determining the spectral profile of the coupled system, which was reported in our previous work [50]. The noise operator $\hat{F}$ overrides the background fluctuations from the Monte Carlo simulation.

For the present coupling system, the dispersion and damping rates of the QBIC modes were obtained by fitting the simulated transmission spectra with Eq. (2). We need to consider only the radiative damping rate of the QBIC mode while ignoring the nonradiative damping because of the extremely weak Ohmic losses in the all-dielectric system. In addition, the linewidth of the temperature-controlled QBIC mode greatly affects the incoherent damping rate, which also determines the ultrafast dynamics of the subsystem. This will be explored in more detail next.

Inserting the eigenvalues solved by Eq. (3) into Eq. (5) with the coherent and incoherent coupling strengths for 30 °C ($\hbar g$ = 14 meV and $\hbar\gamma=0.4$ meV) and 80 °C ($\hbar g=10.5$ meV and $\hbar\gamma=1.2$ meV), we calculate the static spectra as a function of θ, as shown in Figs. 4(a) and 4(b). The calculated transmission spectra obtained with the quantum model agree well with the simulation results. Importantly, the coherent coupling strength $\hbar g$ is positive at both 30 °C and 80 °C, i.e., $\phi=0°$, which reveals that the temperature does not induce a shift in the initial phase of the QBIC mode. This can be verified by the near-field distribution of the QBICs modes at different temperatures, as shown in Fig. 2(e), plots (i)–(iii).

To further investigate the coherent and incoherent QBIC-exciton coupling dynamics, we calculate the populations of the hybrid modes evolving in the time domain. For the sake of comparison, we will focus on only the population evolution at zero detuning. Under Gaussian optical excitation, we calculate the temporal population dynamics of the QBIC modes and excitons in the LP branch for the coupled system for 30 °C and 80 °C, as shown in Figs. 4(c) and 4(d), respectively. We note that the population between the QBIC mode and the exciton exhibits a periodic transfer and lasts for more than 1000 fs for the case of 30 °C. The vertical gray dashed line explicitly labels the Rabi period $T=$ 158 fs, which in turn proves that the coherent coupling strength between the QBIC and the exciton is $\hbar g=14$ meV ($T=\pi/g$). In contrast, for the case of 80 °C, population exchange lasts less than two Rabi periods up to 200–400 fs and then damps away. This is attributed to the reduced coupling strength of the system. In addition,

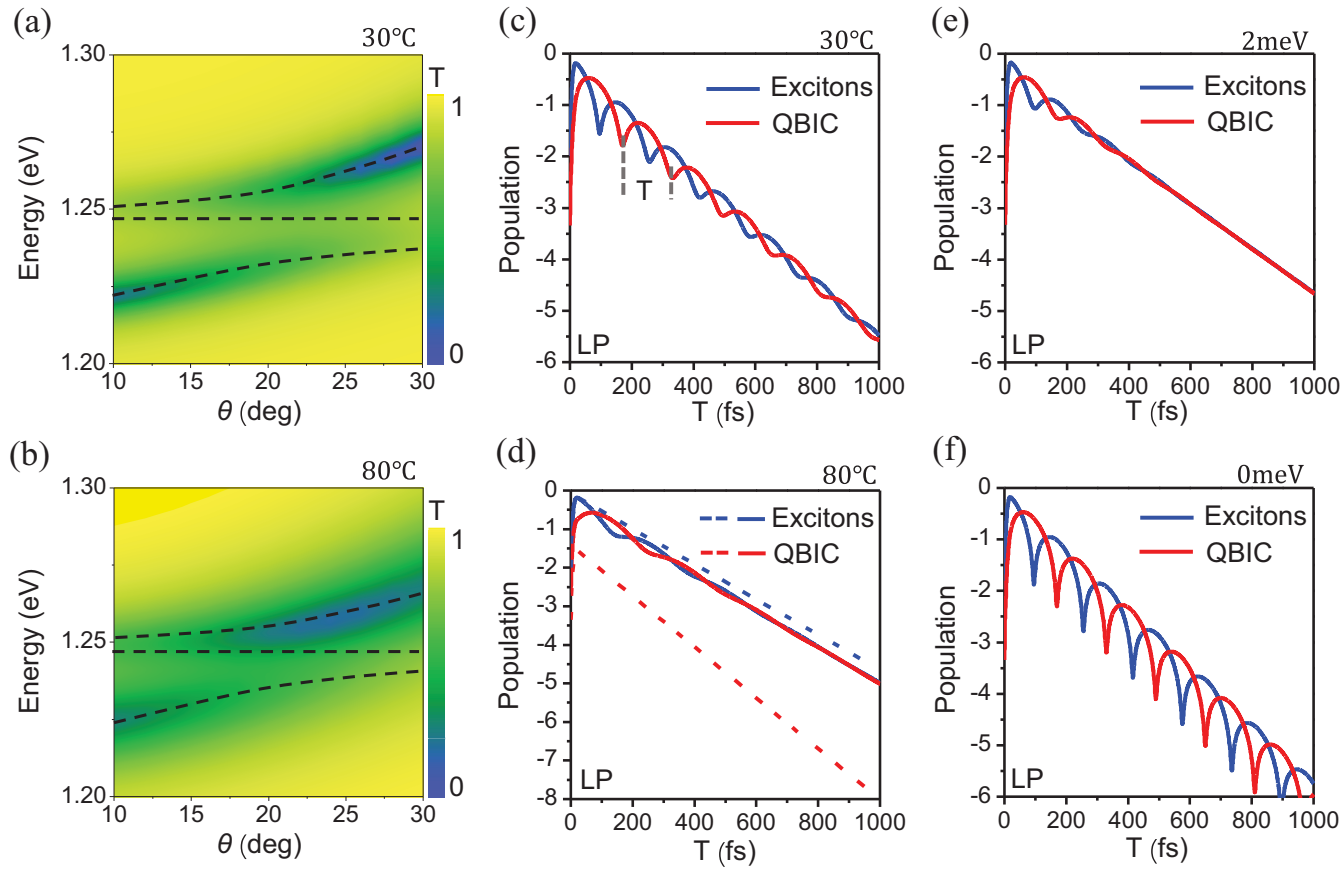

FIG. 4. The transmission spectrum of the coupling system as a function of asymmetric parameter θ (in color scale) at (a) 30 °C and (b) 80 °C obtained with the quantum model. Time-domain evolution of the QBIC (red) and exciton (blue) populations in LP at zero detuning for coupled systems at (c) 30 °C and (d) 80 °C. The red and blue dotted lines represent the populations of independent QBICs and excitons, respectively, evolving over time. The time-domain evolution of QBIC (red) and excitons (blue) populations in the LP for incoherent coupling strength (e) $\hbar\gamma_c = 2$ meV and (f) $\hbar\gamma_c = 0$ meV when the temperature of the coupling system is 30 °C.

we present the population evolution before QBIC modes and exciton coupling, shown by the blue and red dashed lines in Fig. 4(d), respectively. The quite apparent change is that the population evolution of QBICs and excitons after coupling is essentially the same as the population of QBIC modes before coupling, which is attributed to the lifetime of the polariton states being limited to the shortest lifetime of the two subsystems.

To fully understand the longer coherence times for 30 °C with respect to those for 80 °C, we first recall the coupling-induced incoherent damping term $\hbar\gamma$ between individual subsystem via the continuum reservoir because it is directly related to the population damping rate. Figures 4(e) and 4(f) demonstrate the temporal population evolution of the QBIC and exciton mode in the LP for 30 °C with $\hbar\gamma = 2$ meV and $\hbar\gamma = 0$ meV, respectively. Apparently, the coherence time between the QBIC and the exciton is drastically shortened when the incoherent damping rate increases from 0 to 2 meV. Essentially, this occurs because the time-translation symmetry of the QBIC mode and exciton population fractions is broken when the incoherent damping rate $\hbar\gamma \neq 0$. If the QBIC modes and excitons have only coherent interaction channels without incoherent damping pathways ($\hbar\gamma = 0$), the time-translation symmetry of the subsystem will always hold, which results in sustained coherence times without decay, as shown in Fig. 4(f). Therefore, we can achieve long coherent lifetimes by decreasing the incoherent damping rate in the hybrid system, which is particularly important in many ultrafast quantum device applications, especially in the fields of quantum computation and quantum information. To reduce the incoherent damping rate of the present coupling system, there are two paths according to $\gamma_c \leqslant \sqrt{\gamma_{\mathrm{Q,rad}}\gamma_{\mathrm{X,rad}}}(\hat{\boldsymbol{\mu}}_{\mathrm{Q}} \cdot \hat{\boldsymbol{\mu}}_{\mathrm{X}})$: (1) lowering the temperature to achieve the long-lived QBIC mode supported by the Si-VO_2 metasurface and (2) tuning the orientation of the effective dipole moment of the QBIC and exciton modes.

E. Concentration-controlled manipulation of coupling strength

It is well known that there are two widely used approaches to improve the coupling strength of a coupled system. One is boosting the electric field strength in optical resonators. The other is enhancing the oscillator strength of the coupling emitters. We demonstrated in the previous section that the electric field strength can be enlarged at QBIC resonance by tuning the temperature. In this section, we will explore the effect of the oscillator strength of the SWCNTs on the coupling strength of the hybrid system.

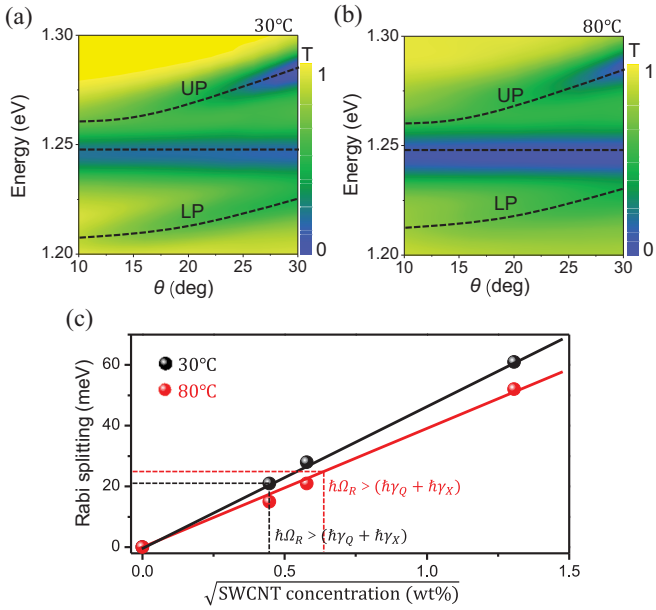

FIG. 5. Simulated transmission spectra of the coupling system as a function of the asymmetric parameter θ (in color scale) at (a) 30 °C and (b) 80 °C when the concentration of SWCNTs is 1.71 wt %. (c) Rabi splitting of the coupling system at different temperatures as a function of the square root of the SWCNT concentration. The transition regimes of the coupling system from the weak to strong coupling condition at temperatures of 30 °C and 80 °C are indicated by black and red dashed lines, respectively.

Generally, the oscillator strength of SWCNTs can be enlarged by increasing the concentration of the SWCNT solution. Figures 5(a) and 5(b) give the simulated transmission spectra as a function of θ with a concentration of 1.71 wt % for 30 °C and 80 °C, respectively. Obviously, the transmission spectra for both 30 °C and 80 °C exhibit a more distinct anticrossing phenomenon compared to those with low concentration [Figs. 3(a) and 3(b)]. From Eq. (3), the Rabi splitting can be evaluated to be $\hbar\Omega = 61$ meV and $\hbar\Omega = 55$ meV for 30 °C and 80 °C, respectively, corresponding to a nearly 3 times greater boosting of the coupling strength with respect to the previous lower-concentration case.

We further quantitatively evaluate the dependence of the Rabi splitting on the oscillator strength of the SWCNTs. Figure 5(c) illustrates the Rabi splitting as a function of the square root of the SWCNT concentration, which exhibits a linear trend for both 30 °C (solid black line) and 80 °C (solid red line). Importantly, we can also quantify the concentration threshold at which the system can be transitioned from the weak to strong coupling regime. According to the determination criteria, i.e., $\hbar\Omega_R > (\hbar\gamma_Q + \hbar\gamma_X)$, the concentration thresholds for weak-to-strong transitions can be evaluated for the cases of 30 °C (dashed black line) and 80 °C (dashed red line), as shown in Fig. 5(c). We can clearly see that strong coupling can be achieved with a minimum concentration of 0.11 wt % for the case of 30 °C. However, for the case of 80 °C, a concentration of at least 0.41 wt % is required to enable the weak-to-strong transition. We note that the Rabi splittings are enlarged linearly with increasing SWCNT concentration more than 1 wt %. Therefore, it is reasonable to predict that the hybrid system can be brought into the ultrastrong coupling regime if we further increase the concentration, which may offer an efficient way of probing ultrastrong light-matter interactions in the near-infrared communication band.

III. CONCLUSIONS

To summarize, we proposed a highly compact and low-loss all-dielectric metasurface combined with the PCM material VO_2, enabling an active tuning of SWCNT-based exciton-QBIC coupling in the NIR region. We demonstrated control of the exciting QBIC by changing temperatures, successfully achieving an active and flexible tuning of exciton-QBIC interactions. A multipole expansion approach combined with near-field analysis was employed, revealing that the magnetic dipole and high-order electric quadrupole are dominate at QBIC resonance with significant field enhancement, thus greatly facilitating the exciton-QBIC interaction. A quantum model based on Heisenberg-Langevin formalism was also used to fully describe the microscopic coupling dynamics, demonstrating a temperature-dependent sub- and superradiance of the polariton states. We finally demonstrated a linear dependence of the exciton-QBIC coupling strength on the SWCNT concentration. Our work represents a promising pathway towards practical polariton devices operating at the telecommunication wavelength.

ACKNOWLEDGMENT

This work was supported by the National Natural Science Foundation of China (Grant No. 11974254).

[1] P. Torma and W. L. Barnes, Rep. Prog. Phys. **78**, 013901 (2015).
[2] K. Hennessy, A. Badolato, M. Winger, D. Gerace, M. Atature, S. Gulde, S. Falt, E. L. Hu, and A. Imamoglu, Nature (London) **445**, 896 (2007).
[3] L. J. Huang, A. Krasnok, A. Alu, Y. L. Yu, D. Neshev, and A. E. Miroshnichenko, Rep. Prog. Phys. **85**, 046401 (2022).
[4] W. Wang, P. Vasa, R. Pomraenke, R. Vogelgesang, A. De Sio, E. Sommer, M. Maiuri, C. Manzoni, G. Cerullo, and C. Lienau, ACS Nano **8**, 1056 (2014).
[5] J. Kasprzak, M. Richard, S. Kundermann, A. Baas, P. Jeambrun, J. M. J. Keeling, F. M. Marchetti, M. H. Szymanska, R. Andre, J. L. Staehli, V. Savona, P. B. Littlewood, B. Deveaud, and L. S. Dang, Nature (London) **443**, 409 (2006).
[6] P. Bhattacharya, T. Frost, S. Deshpande, M. Z. Baten, A. Hazari, and A. Das, Phys. Rev. Lett. **112**, 236802 (2014).
[7] N. G. Berloff, M. Silva, K. Kalinin, A. Askitopoulos, J. D. Topfer, P. Cilibrizzi, W. Langbein, and P. G. Lagoudakis, Nat. Mater. **16**, 1120 (2017).
[8] H. Deng, H. Haug, and Y. Yamamoto, Rev. Mod. Phys. **82**, 1489 (2010).
[9] L. Y. Sun, C. Y. Wang, A. Krasnok, J. Choi, J. W. Shi, J. S. Gomez-Diaz, A. Zepeda, S. Gwo, C. K. Shih, A. Alu, and X. Q. Li, Nat. Photon. **13**, 180 (2019).

[10] M. D. Fraser, S. Hofling, and Y. Yamamoto, Nat. Mater. **15**, 1049 (2016).
[11] P. L. Hong, L. Xu, and M. Rahmani, Opto-Electron. Adv. **5**, 200097 (2022).
[12] S. Christopoulos, G. Baldassarri Höger von Högersthal, A. J. D. Grundy, P. G. Lagoudakis, A. V. Kavokin, J. J. Baumberg, G. Christmann, R. Butté, E. Feltin, J. F. Carlin, and N. Grandjean, Phys. Rev. Lett. **98**, 126405 (2007).
[13] X. Z. Liu, T. Galfsky, Z. Sun, F. N. Xia, E. C. Lin, Y. H. Lee, S. Kena-Cohen, and V. M. Menon, Nat. Photon. **9**, 30 (2015).
[14] M. Sidler, P. Back, O. Cotlet, A. Srivastava, T. Fink, M. Kroner, E. Demler, and A. Imamoglu, Nat. Phys. **13**, 255 (2017).
[15] W. Liu, B. Lee, C. H. Naylor, H.-S. Ee, J. Park, A. T. C. Johnson, and R. Agarwal, Nano Lett. **16**, 1262 (2016).
[16] J. Cuadra, D. G. Baranov, M. Wersall, R. Verre, T. J. Antosiewicz, and T. Shegai, Nano Lett. **18**, 1777 (2018).
[17] K. As'ham, I. Al-Ani, L. J. Huang, A. E. Miroshnichenko, and H. T. Hattori, ACS Photonics **8**, 489 (2021).
[18] R. B. Weisman and S. M. Bachilo, Nano Lett. **3**, 1235 (2003).
[19] X. J. Zhou, J. Y. Park, S. M. Huang, J. Liu, and P. L. McEuen, Phys. Rev. Lett. **95**, 146805 (2005).
[20] X. Ma, N. F. Hartmann, J. K. S. Baldwin, S. K. Doorn, and H. Htoon, Nat. Nanotechnol. **10**, 671 (2015).
[21] S. Khasminskaya, F. Pyatkov, B. S. Flavel, W. H. Pernice, and R. Krupke, Adv. Mater. **26**, 3465 (2014).
[22] R. Miura, S. Imamura, R. Ohta, A. Ishii, X. Liu, T. Shimada, S. Iwamoto, Y. Arakawa, and Y. K. Kato, Nat. Commun. **5**, 5580 (2014).
[23] F. Pyatkov, V. Fuetterling, S. Khasminskaya, B. S. Flavel, F. Hennrich, M. M. Kappes, R. Krupke, and W. H. P. Pernice, Nat. Photon. **10**, 420 (2016).
[24] R. Watahiki, T. Shimada, P. Zhao, S. Chiashi, S. Iwamoto, Y. Arakawa, S. Maruyama, and Y. K. Kato, Appl. Phys. Lett. **101**, 141124 (2012).
[25] Y. Zakharko, A. Graf, S. P. Schiessl, B. Hähnlein, J. Pezoldt, M. C. Gather, and J. Zaumseil, Nano Lett. **16**, 3278 (2016).
[26] Y. Zakharko, A. Graf, and J. Zaumseil, Nano Lett. **16**, 6504 (2016).
[27] A. Graf, L. Tropf, Y. Zakharko, J. Zaumseil, and M. C. Gather, Nat. Commun. **7**, 13078 (2016).
[28] M. Son, Z. T. Armstrong, R. T. Allen, A. Dhavamani, M. S. Arnold, and M. T. Zanni, Nat. Commun. **13**, 7305 (2022).
[29] C. Moehl, A. Graf, F. J. Berger, J. Luettgens, Y. Zakharko, V. Lumsargis, M. C. Gather, and J. Zaumseil, ACS Photonics **5**, 2074 (2018).
[30] A. Dhavamani, L. Haeberle, J. Wang, S. Kena-Cohen, and M. S. Arnold, ACS Photonics **8**, 2375 (2021).
[31] J. M. Luettgens, Z. Kuang, N. F. Zorn, T. Buckup, and J. Zaumseil, ACS Photonics **9**, 1567 (2022).
[32] P. Xie, Q. Ding, Z. Liang, S. Shen, L. Yue, H. Zhang, and W. Wang, Phys. Rev. B **107**, 075415 (2023).
[33] P. Xie, Y. H. Deng, L. X. Zeng, Z. C. Liang, S. Y. Shen, Q. Ding, H. Zhang, Z. K. Zhou, and W. Wang, Phys. Rev. B **106**, 165408 (2022).
[34] V. Kravtsov, E. Khestanova, F. A. Benimetskiy, T. Ivanova, A. K. Samusev, I. S. Sinev, D. Pidgayko, A. M. Mozharov, I. S. Mukhin, M. S. Lozhkin, Y. V. Kapitonov, A. S. Brichkin, V. D. Kulakovskii, I. A. Shelykh, A. I. Tartakovskii, P. M. Walker, M. S. Skolnick, D. N. Krizhanovskii, and I. V. Iorsh, Light: Sci. Appl. **9**, 8 (2020).
[35] N. Bernhardt, K. Koshelev, S. J. U. White, K. W. C. Meng, J. E. Froch, S. Kim, T. Toan Trong, D.-Y. Choi, Y. Kivshar, and A. S. Solntsev, Nano Lett. **20**, 5309 (2020).
[36] A. Elbanna, K. Chaykun, Y. Lekina, Y. Liu, B. Febriansyah, S. Li, J. Pan, Z. X. Shen, and J. Teng, Opto-Electron. Sci. **1**, 220006 (2022).
[37] C. Fang, Q. Yang, Q. Yuan, X. Gan, J. Zhao, Y. Shao, Y. Liu, G. Han, and Y. Hao, Opto-Electron. Adv. **4**, 200030 (2021).
[38] K. L. Sun, M. Sun, Y. J. Cai, U. Levy, and Z. H. Han, Nanophotonics **11**, 4221 (2022).
[39] M. Shahzadi, C. Y. Zheng, S. Ahmad, S. S. Wang, and W. L. Zhang, Opto-Electron. Adv. **5**, 200066 (2022).
[40] L. Liu, R. Wang, Y. Sun, Y. Jin, and A. Wu, Nanophotonics **12**, 3159 (2023).
[41] S. T. Ha, R. Paniagua-Dominguez, and A. I. Kuznetsov, Adv. Opt. Mater. **10**, 2200753 (2022).
[42] I. A. M. Al-Ani, K. As'Ham, L. Huang, A. E. Miroshnichenko, and H. T. Hattori, Laser Photonics Rev. **15**, 2100240 (2021).
[43] I. A. M. Al-Ani, K. As'Ham, M. Alaloul, L. Xu, H. T. Hattori, L. Huang, and A. E. Miroshnichenko, Phys. Rev. B **108**, 045420 (2023).
[44] C. G. Gao, S. J. You, Y. Zhang, L. L. Wang, H. Duan, H. X. He, Q. Xie, and C. B. Zhou, Appl. Phys. Lett. **124**, 051701 (2024).
[45] M. B. Qin, J. Y. Duan, S. Y. Xiao, W. X. Liu, T. B. Yu, T. B. Wang, and Q. H. Liao, Phys. Rev. B **105**, 195425 (2022).
[46] A. Tripathi, S. Kruk, J. John, Z. Zhang, H. S. Nguyen, L. Berguiga, P. R. Romeo, R. Orobtchouk, S. Ramanathan, Y. Kivshar, and S. Cueff, ACS Photonics **8**, 1206 (2021).
[47] K. Koshelev, S. Lepeshov, M. K. Liu, A. Bogdanov, and Y. Kivshar, Phys. Rev. Lett. **121**, 193903 (2018).
[48] P. Xie, Z. C. Liang, T. T. Jia, D. M. Li, Y. X. Chen, P. J. Chang, H. Zhang, and W. Wang, Phys. Rev. B **104**, 125446 (2021).
[49] P. Xie, Z. Liang, Z. Li, W. Wang, W. Wang, T. Xu, X. Kuang, L. Qing, D. Li, and J. Yi, Phys. Rev. B **101**, 045403 (2020).
[50] Z. C. Liang, L. Y. Qing, Z. J. Li, X. T. Nguyen, T. Xu, A. De Sio, H. Zhang, C. Lienau, and W. Wang, Phys. Rev. B **102**, 035422 (2020).